Generation of Dense and High-Precision Digital Elevation Model Using Low-Cost Unmanned Aerial Vehicle and Space-Borne TanDEM-X to Measure Exposed Area Change Due to Tidal Invasion

Hyoseong Lee and Duk-jin Kim, *Senior Member, IEEE*

***Abstract*—Tidal flats are internationally protected areas because of their environmental, geological, and economic value. Nevertheless, these are areas where casualties are common among visitors. To ensure the safety of visitors, efforts must be made to understand the geomorphologic characteristics of tidal flats. It is necessary to use three-dimensional (3-D) topographic data to clearly determine when an exposed tidal flat rapidly disappears as a result of periodic tidal fluctuations. Digital elevation models (DEMs) created using unmanned aerial vehicle (UAV) imaging and commercial photogrammetric software to measure tidal flats are produced using ground control points (GCPs). It is difficult to conduct field surveys and readings of image coordinates that correspond to these because tidal flat areas are difficult to access. The distribution of GCPs affects the accuracy of a DEM because the entire test region cannot be covered during a survey. Without GCPs, the DEM generated with the UAV images and photogrammetric software using the structure from the motion technique probably has nonlinear distortion such as a bowl shape. This article proposes a practical method of least-squares 3-D surface matching with a polynomial model (LS3D-PM) to correct a distorted DEM. For this LS3D-PM matching, a global TanDEM-X DEM was used instead of a field survey to collect the GCPs in a tidal flat. Practical testing was conducted using the proposed method. The root-mean-square error with respect to the height decreased from approximately 1.0 to 0.1 m, and the bowl-effect error was eliminated. With the DEM corrected using the proposed method and the classified orthoimages, the exposed tidal flat changes due to seawater invasion were estimated at different times during flood tide. This method has nontrivial technical values for quick and relatively precise DEM generations at a low cost compared to that of other techniques, particularly in emergency situations such as tsunamis, landslides, and earthquakes.**

***Index Terms*—Bowl effect, digital elevation model (DEM), least-squares 3-D surface matching with a polynomial model (LS3D-PM), seawater changes, TanDEM-X, tidal flat.**

Manuscript received 17 February 2022; revised 20 May 2022 and 27 June 2022; accepted 19 July 2022. Date of publication 2 August 2022; date of current version 29 August 2022. This work was supported in part by the Ministry of Education of the Republic of Korea and the National Research Foundation of Korea under Grant NRF-2018R1D1A1B06049484 and in part by the Disaster-Safety Industry Promotion Program under Grant 2019-MOIS32-015 funded by the Ministry of Interior and Safety. *(Corresponding author: Duk-jin Kim.)*

Hyoseong Lee is with the Department of Civil Engineering, Sunchon National University, Sunchon 57922, South Korea (e-mail: hslee@scnu.ac.kr).

Duk-jin Kim is with the School of Earth and Environmental Sciences, Seoul National University, Seoul 08826, South Korea (e-mail: djkim@snu.ac.kr).

Digital Object Identifier 10.1109/JSTARS.2022.3195744

I. Introduction

TIDAL flats are unique ecological places on Earth because they are submerged in water during high tide and fully exposed during low tide. These areas are wetlands that form within coastal regions when tides or rivers deposit sand or mud. This phenomenon produces economically valuable and environmentally healthy geographical features because rivers supply sediment and organic matter, supporting a diverse ecosystem [1]. These areas also have significant value in terms of habitat for shellfish, water purification, the maintenance of diverse species, flood control, and recreational and scenic resources [1]. A tidal flat is also an internationally protected shelter for endangered migratory birds and is considered to be a rich ecosystem with a wide range of species [2].

Many tourists visit and experience tidal flats every year because of the value of such flats. However, they can be dangerous places for humans to access because their uniquely muddy topographic features are submerged and exposed approximately twice daily. Humans have difficulty moving around under these conditions and can easily become stuck during a rising tide. The most critical part of a tidal environment's topography is the tidal channels, which are narrow inlets or estuaries that are affected by the ebb and flow of ocean tides.

A tidal channel serves to transport not only nutrients and organic matter but also sediment and has topographical features that determine the sedimentation pattern of the entire tidal flat. Several studies have been conducted on the changes in the width, depth, and velocity of a tidal channel with the discharge at various cross sections and along the length of the channel, showing that estuarine channels differ from terrestrial channels [4], [5].

Despite this valuable role, as the tide rises, seawater flows into the bank until it overflows levees and becomes a sheet flow, making it a potential hazard for humans. These conditions led to 310 reported casualties in South Korea from 2017 to 2020 [3]. To consider the safety of visitors, attention must be given to tidal flats to understand their geomorphologic characteristics. They need to be mapped in three dimensions (3-D) to account for the rapidly invaded areas caused by periodic tidal fluctuations.

The difficulty in accessing tidal flats hinders traditional terrestrial topographic surveying methods, making it necessary to

collect data remotely to map a tidal flat. Various types of remote sensors are available for the topographic mapping of tidal flats, including optical satellite sensors, satellite radar sensors, aerial cameras, airborne light detection and ranging (LiDAR) devices, and echo sounders [6]–[8]. Each sensor has its own advantages and disadvantages. Satellite sensors have a large swath that enables the cost-effective mapping of large target areas, but they provide lower spatial resolution than aerial cameras. Aerial cameras provide higher spatial resolution with high geometric accuracy, but their operational costs are high, and their use is limited by severe weather and flight restrictions. The Korea Hydrographic and Oceanographic Agency created topographic data for tidal flats across the Korean Peninsula using LiDAR to prevent tidal flat accidents [9]. However, it is difficult to measure tidal flats twice a day. Moreover, measurements using a LiDAR system are expensive and involve many processing tasks; thus, the system does not work adequately in the case of tidal flats because seawater puddles can remain even after they are exposed [10], [11]. The use of echo sounders is also unsuitable because a ship carrying hull-mounted sonar cannot conduct a survey in special cases of very shallow water levels such as those found in intertidal flats.

First, to prevent casualties in advance and provide an hourly profile that can visibly inform visitors of the time of tidal flat exposure risk, it is necessary to measure the water level and surface area of the tidal channel by securing high-resolution digital elevation models (DEMs) and orthoimages for each time period. In this regard, several studies have examined the possibility of generating the topography of a tidal flat using unmanned aerial vehicle (UAV) images and commercial photogrammetric software such as Agisoft PhotoScan (current software version is Metashape) or Pix4D, utilizing the structure from motion (SfM) technique. According to these studies, on-site ground control points (GCPs) are required for the accurate development of a DEM [12]–[14]. A survey of the GCPs was still difficult because it was not easy to approach the tidal flats on the southwest coast of the Korean peninsula, where the silt and clay contents are high [15].

Without GCPs, a DEM generated using UAV images and photogrammetric software had location errors. It was also likely to contain nonlinear distortion that overestimated the elevation of the terrain. The systematic overvaluation of the terrain increased with the distance from the center as a result of the "bowl or doming effect" [16]–[18], which affected the external area covered by the GCPs [19], [20]. Additionally, there is a high possibility that the bowl effect will occur for a DEM based on the images of narrow and long areas such as tidal channels acquired by a UAV during a long flight [20], [21]. The bowl effect is probably caused by the inaccurate self-calibration of SfM-based software with no GCPs and an unstable rolling shutter [21]. Therefore, the DEMs distorted by the bowl effect for each time period should be corrected to measure the water level and surface area of a tidal channel using UAVs while avoiding GCP field surveying.

Recently, UAVs with integrated onboard real-time kinematics (RTK) have been used for terrain mapping. On the other hand, an assessment of the accuracy of DEMs revealed an average root-mean-square error (RMSE) of approximately 0.5–2.0 m, depending on the imaging direction (nadiral or oblique), without GCPs when a DJI Phantom 4 RTK was flown on a north-to-south trajectory over a 2-km coastal site [22], [23]. The base station must be defined even if no GCP needs to be surveyed, particularly in inaccessible areas. It is possible to precisely georeferenced the position of the UAV images.

Although this effect can be removed through sophisticated imaging technology with the UAV-based RTK option, we preferred to correct the UAV DEM in a more practical and cost-effective way. Because the tidal flats formed along the coastline are prone to frequent gusts of wind, there was a high risk of damage to a UAV equipped with an integrated on-board RTK with a survey-grade global navigation satellite system (GNSS) receiver. Thus, we used a low-cost UAV.

This study had the goal of correcting the distorted UAV DEM by applying a 3-D matching technique using an existing reference DEM such as LiDAR, global DEM (elevation data representing the worldwide terrain) or precompensated dense DEM, instead of the GCPs. A well-known approach to 3-D matching in the two datasets is the iterative closest point (ICP) method for nontarget registration [24]. The ICP method is based on a search for pairs of the nearest points in the two datasets and an estimation of the rigid transformation that aligns them. Another powerful approach to improve 3-D matching is least-squares 3-D (LS3D) surface matching. This approach was designed for arbitrary 3-D surface data and is an extension of 2-D least-squares image matching [25].

A DEM produced using the UAV images with no RTK and GCP included 3-D location error, 3-D rotation error, scale error, and overall nonlinear distortion owing to the bowl effect. Therefore, even if three shifts, three rotations, and scale factors were applied using the reference DEM, the parabolic-nonlinear distortion caused by the bowl effect would not be removed. To overcome this problem, Lee and Han [26] proposed least-squares height-difference (LHD) matching with a polynomial model. They used a LiDAR DEM as a reference DEM to correct the bowl-shaped deformation of the DEM produced using UAV images.

The LHD matching approach estimates the transformation parameters between the two DEMs, which consisted of a 3-D rotation and 3-D translation, as well as a scale parameter. Thus, the sum of the squared height differences was minimized. However, the transformation parameters were less accurate because the LHD matching performance decreased with a decrease in the slope of the DEM. In particular, planimetric parameters in translations depend exclusively on the effect of the slope [27].

This article proposes an LS3D matching method with a polynomial model (called LS3D-PM matching) to rectify the distorted UAV DEM. This concept estimates the 3-D similarity transformation parameters to minimize the distances along the surface normals between the two DEMs. This is different from the LHD, which minimizes the height differences between the two DEMs. It is possible that the LHD transformation becomes ill-posed in situations with large slopes. In contrast, the LS3D model gets stronger with increasing slope angles [28]. Therefore,

the LS3D-PM is more robust than the LHD method, on the large sloped area such as a tidal-channel landform.

In addition, we employed a worldwide TanDEM-X (TerraSAR-X add-on for digital elevation measurement) DEM as the reference DEM. A LiDAR system has the advantage of producing a high-resolution and highly accurate dataset using an aircraft, but it is not available globally because of its high acquisition cost and irregular data acquisition limitations imposed by the conditions of the aircraft's internal equipment [GNSS, inertial navigation system (INS), etc.] and the weather. The TanDEM-X DEM is independent of the weather and offers a viable option for producing a global DEM of the Earth's surface. It also has the advantages of regular data acquisition and covering a wide area, but it has a resolution of approximately 10 m with an RMSE of less than 1.4 m in height, which is lower spatial resolution and accuracy value than those of a LiDAR DEM [29]. Nevertheless, it was worth evaluating whether UAV DEMs could be corrected using these data.

To measure the seawater change during high tide at a tidal channel, DEMs of the tidal flat were produced using UAV overlap-images taken at multiple time intervals and commercial software. The change in seawater, according to the time, was analyzed using the classified orthoimages, and the DEMs were corrected using the proposed method.

This study focused on suggesting an LS3D-PM using TanDEM-X DEM as a reference DEM, which is more stable than LHD and more applicable than a LiDAR DEM, as mentioned above, to secure an accurate tidal flat DEM in a region where a GCP survey was difficult. Therefore, a classification for estimating the seawater changes of a tidal flat was attempted on a trial basis, and the classification accuracy was not analyzed.

II. DEM Correction With Proposed Technique

To measure the change in tidal seawater using UAV images, DEMs and orthoclassified images should be produced at different times. However, the DEM obtained using low-cost UAV images produced without the RTK and GCP option was distorted. In particular, if there were no GCPs, the bowl effect was likely to occur because of error propagation through the inaccurate bundle-adjustment process between the overlapping images and inaccurate self-calibration of the nonmetric camera, as well as the rolling shutter problem in the image space [16]–[21]. This article presents a new approach. The LS3D-PM matching technique was applied using polynomial models of the transformation parameters as a function of grid spaces between the two DEMs to overcome this problem [e.g., Fig. 1(a)]. The objective of this study was to compensate for the DEM using LS3D-PM matching and estimate seawater changes in the tidal channels using orthoclassified images. Based on the proposed approach, Fig. 1(b) shows a flowchart of the processing steps used in the experimental investigations.

In partial regions of the same object area, let $f(x, y, z)$ and $g(x, y, z)$ denote the conjugate surfaces in the TanDEM-X DEM and UAV DEM, respectively. Because the geometric relationship between the two surfaces is not ideally the same state, it includes the effects of random errors. Therefore, an error vector,

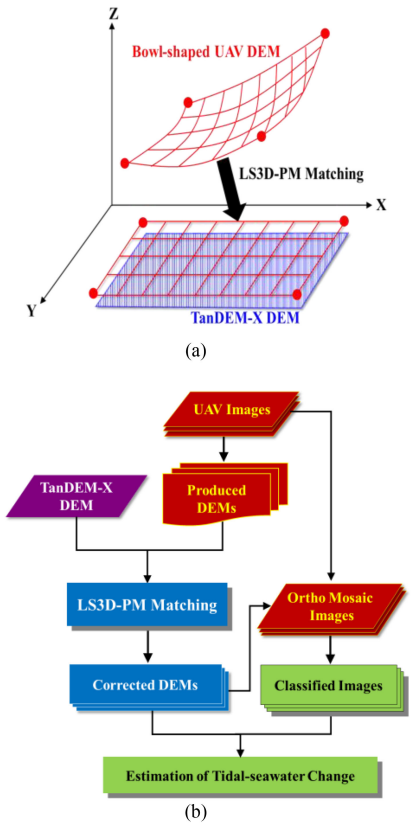

Fig. 1. (a) Illustration of LS3D-PM matching between TanDEM-X DEM and UAV DEM. (b) Flowchart for the correction of a UAV DEM with the proposed LS3D-PM matching and estimation of seawater change.

$e(x, y, z)$, is added between the surfaces as follows:

$$f_i\ (x,\ y,\ z) - e_i\ (x,\ y,\ z) = g_i\ (x,\ y,\ z) \tag{1}$$

where i indicates the ith point.

The matching approach aimed to find the transformation between two surfaces. It consisted of a 3-D translation and 3-D rotation, as well as a scale parameter to minimize the sum of the squared distances between the two surfaces. A seven-parameter 3-D similarity transformation was used to express the geometric relationship between the TanDEM-X DEM and UAV DEM points

$$[x\ y\ z]_i^T = sR\,[x_o\ y_o\ \ z_o]_i^T + t \tag{2}$$

where $R = R(\omega, \varphi, \kappa)$ is the 3-D rotation matrix, $t = [t_x\ \ t_y\ \ t_z]^T$ is a 3-D translation vector, s is a scale factor, $[x,\ y,\ z]_i$ is the location of the $\mathrm{TanDEM-X\ DEM}$, and $[x_o\ y_o\ z_o]_i$ is the location of the conjugate approximate surface, $g_i^o(x,\ y,\ z)$, of the UAV DEM.

In this implementation, (2) is expanded with cubic polynomial parameters to eliminate the bowl-shape distortion of the UAV DEM as follows:

$$t_x = t_{x0}\ + t_{x1}l + t_{x2}l^2 + t_{x3}l^3$$
$$t_y = t_{y0}\ + t_{y1}l + t_{y2}l^2 + t_{y3}l^3$$
$$t_z = t_{z0} + t_{z1}l + t_{z2}l^2 + t_{z3}l^3$$

$$\omega = \omega_0 + \omega_1 l + \omega_2 l^2 + \omega_3 l^3$$
$$\varphi = \varphi_0 + \varphi_1 l + \varphi_2 l^2 + \varphi_3 l^3$$
$$\kappa = \kappa_0 \ + \ \kappa_1 l + \kappa_2 l^2 + \ \kappa_3 l^3 \tag{3}$$

where l is the line and grid space of the DEM, the direction of which is the same as the flight path of the UAV; and $t_x,\ t_y,\ t_z,\ \omega,\ \varphi,$ and κ are polynomial parameters of the transformation according to the grid lines. Depending on the deformation of the UAV surface, any other type of polynomial parameter could be used, e.g., the first to third polynomial parameters for transformation.

To perform a least-squares estimation, (1) should be linearized using the Taylor series (omitting index *i* for simplicity)

$$\begin{aligned} f\,(x,\ y,\ z)\ - e\ (x,\ y,\ z) = g^o\ (x,\ y,\ z) \\ + \frac{\partial g^o\,(x,\ y,\ z)}{\partial x} dx \\ + \frac{\partial g^o\,(x,\ y,\ z)}{\partial y} dy \\ + \frac{\partial g^o\,(x,\ y,\ z)}{\partial z} dz \end{aligned} \tag{4}$$

with

$$g_x = \frac{\partial g^o\,(x,\ y,\ z)}{\partial x} \ = \frac{n_x}{|n|}$$
$$g_y = \frac{\partial g^o\,(x,\ y,\ z)}{\partial y} \ = \frac{n_y}{|n|}$$
$$g_z = \frac{\partial g^o\,(x,\ y,\ z)}{\partial z} \ = \frac{n_z}{|n|} \tag{5}$$

$$dx \ = \frac{\partial x}{\partial p_k}\, dp_k,\ dy \ = \frac{\partial y}{\partial p_k}\, dp_k,\ dz \ = \frac{\partial z}{\partial p_k}\, dp_k \tag{6}$$

where n is a normal vector of the UAV surface; $n_x,\ n_y\ ,$ and n_z are the x, y, and z components of n, respectively; and $p_k \in \{t_x,\ t_y,\ t_z,\ \omega,\ \varphi,\ \kappa,$ and $s\}$ are the kth transformation parameters in (2) and (3). The differentiation of (2) and (3) yields the following:

$$\begin{aligned} dx = dt_{x0} + \ dt_{x1} l \ + \ dt_{x2} l^2 \ + \ dt_{x3} l^3 \ + \ a_{10} ds \\ + a_{11} d\omega_0 + \ a_{11} d\omega_1 l \ + \ a_{11} d\omega_2 l^2 \ + \ a_{11} d\omega_3 l^3 \\ + a_{12} d\varphi_0 + \ a_{12} d\varphi_1 l \ + \ \ a_{12} d\varphi_2 l^2 \ + \ a_{12} d\varphi_3 l^3 \\ + a_{13} d\kappa_0 \ + \ a_{13} d\kappa_1 l \ + \ \ a_{13} d\kappa_2 l^2 \ + \ a_{13} d\kappa_3 l^3 \\ dy = dt_{y0} \ + \ \ dt_{y1} l \ + \ dt_{y2} l^2 \ + \ dt_{y3} l^3 \ + \ a_{20} ds \\ + a_{21} d\omega_0 + \ a_{21} d\omega_1 l \ + \ a_{21} d\omega_2 l^2 \ + \ a_{21} d\omega_3 l^3 \\ + a_{22} d\varphi_0 + \ a_{22} d\varphi_1 l \ + \ a_{22} d\varphi_2 l^2 \ + \ a_{22} d\varphi_3 l^3 \\ + a_{23} d\kappa_0 \ + \ a_{23} d\kappa_1 l \ + \ a_{23} d\kappa_2 l^2 \ + \ a_{23} d\kappa_3 l^3 \\ dz = dt_{z0} \ + \ \ dt_{z1} l \ + \ dt_{z2} l^2 \ + \ dt_{z3} l^3 \ + a_{30} ds \\ + a_{31} d\omega_0 + \ a_{31} d\omega_1 l \ + \ a_{31} d\omega_2 l^2 \ + \ a_{31} d\omega_3 l^3 \\ + a_{32} d\varphi_0 + \ a_{32} d\varphi_1 l \ + \ a_{32} d\varphi_2 l^2 \ + \ a_{32} d\varphi_3 l^3 \\ + a_{33} d\kappa_0 \ + \ a_{33} d\kappa_1 l \ + \ a_{33} d\kappa_2 l^2 \ + \ a_{33} d\kappa_3 l^3 \end{aligned} \tag{7}$$

where $dt_{xj},\ dt_{yj},\ dt_{zj},\ d\omega_j,\ d\varphi_j,\ d\kappa_j\,(j\ =\ 0,\ \ldots 3)$, and ds are the transformation parameters according to the grid lines of the DEM, the coefficient terms a_{jj} were calculated using partial derivatives with respect to the three rotation angles (ω, φ, κ) in (3).

Equations (5) and (7) are substituted in (4), and the transformation parameters are finally determined using

$$\begin{aligned} & - e\,(x,\ y,\ z) \\ = \ & g_x \ dt_{x0} \ + g_y \ dt_{y0} \ + g_z \ dt_{z0} \\ & + \ g_x \ dt_{x1} \cdot l \ + g_y \ dt_{y1} \cdot l \ + g_z \ dt_{z1} \cdot l \\ & + \ \ g_x \ dt_{x2} \cdot l^2 \ + g_y \ dt_{y2} \cdot l^2 + g_z \ dt_{z2} \cdot l^2 \\ & + \ g_x \ dt_{x3} \cdot l^3 \ + g_y \ dt_{y3} \cdot l^3 + g_z \ dt_{z3} \cdot l^3 \\ & + \ (g_x \ a_{10} \ + g_y \ a_{20} \ + g_z \ a_{30})\ ds \\ & + \ \ b_1 \cdot d\omega_0 + \ b_1 \cdot d\omega_1 \cdot l \ + \ b_1 \cdot d\omega_2 \cdot l^2 \ + \ b_1 \cdot d\omega_3 \cdot l^3 \\ & + \ \ b_2 \cdot d\varphi_0 + \ b_2 \cdot d\varphi_1 \cdot l \ + \ \ b_2 \cdot d\varphi_2 \cdot l^2 \ + \ b_2 \cdot d\varphi_3 \cdot l^3 \\ & + \ \ b_3 \cdot d\kappa_0 \cdot + b_3 \cdot d\kappa_1 \cdot l \ + \ \ b_3 \cdot d\kappa_2 \cdot l^2 \ + \ \ b_3 \cdot d\kappa_3 \cdot l^3 \\ & - \ (f\ \ (x,\ y,\ z) - g^o\,(x,\ y,\ z)) \end{aligned} \tag{8}$$

where $b_1 = (g_x a_{11} + g_y a_{21} + g_z a_{31})\ ,\ \ b_2 = (g_x a_{12} + g_y a_{22} + g_z a_{32}) \quad ,\ b_3 = (g_x\ a_{13} + g_y a_{23} + g_z a_{33}) \quad ,$ and $L \ = \ (f\ (x,\ y,\ z) - g^o(x,\ y,\ z))$ are the normal distances between TanDEM-X and the corresponding surface elements of the UAV DEM. In the present implementation, to determine the normal distance from a point on the UAV surface to a TanDEM-X surface point, the UAV surface points ($g^o(x,\ y,\ z)$) were calculated using bilinear interpolation.

If the transformation parameters are written as a vector of unknowns X, the partial derivatives are design matrix A, and the distances between the two surface elements is the vector of observations L, then the linearized correction equations are given as follows:

$$-e_{(i,1)} = A_{(i,m)}\ \mathrm{X}_{(m,1)} - L_{(i,1)} \tag{9}$$

where $\mathrm{X}^{\mathrm{T}} = [dt_{xj},\ dt_{yj},\ dt_{zj},\ d\omega_j,\ d\varphi_j,\ d\kappa_j,$ and $ds]$, and m is the number of unknown parameters. Then, (9) can be expressed in a least-squares form to calculate parameters $dt_{xj},\ dt_{yj},\ dt_{zj},\ d\omega_j,\ d\varphi_j,\ d\kappa_j,$ and ds as follows:

$$\mathrm{X} \ = \left(A^T P A\right)^{-1}\ \left(A^T P L\right). \tag{10}$$

LS3D-PM matching uses the normal distance between two DEMs. The distance (d_i) of any point (i) must not be significantly different from those of the other points. Therefore, a simple weighting scheme is adopted

$$P \ = \begin{cases} 1 \text{ if } \ |d_i - \text{mean}\,(d_i)| < 1.0\sigma \\ 0 \text{ else} \end{cases}. \tag{11}$$

To eliminate the gross error point and outliers, only the point where d_i is within 1.0σ (σ is the standard deviation of d_i) can

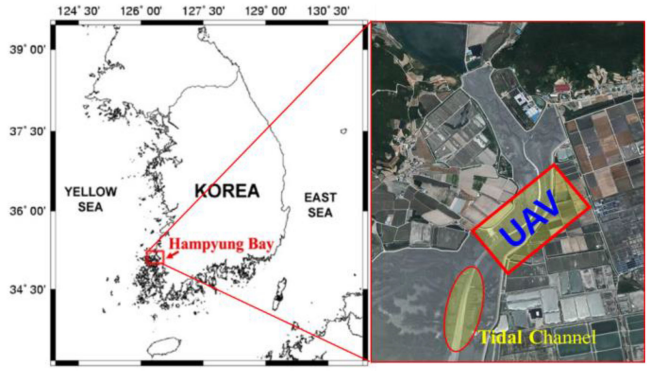

Fig. 2. Map of Korean peninsula (left) with UAV imaging area (right) in Hampyung Bay used for the test.

participate in matching. The transformation parameters were then determined until the X terms were nearly zero. The adjustment equations had to be solved iteratively. In every iteration, the unknowns were updated using the results from (10), such as $t^1_{xj} = t^0_{xj} + dt_{xj}$, $t^1_{yj} = t^0_{yj} + dt_{yj}$, ... The convergence behavior of the proposed method relies on the quality of the initial approximations and quality of the data content.

Orthomosaic images were produced using the corrected DEMs. Using these images, classification images were obtained using the maximum-likelihood method. The large changes in the water surface were then measured using the corrected DEMs for different times. The seawater areas were calculated using the classified images. Finally, the seawater changes in the tidal channel were determined using the corrected DEMs and classified images.

III. Experimental Investigations and Results

The test site for the experiments was a tidal flat area in Hampyung Bay, which is located on the west coast of the Korean Peninsula (see Fig. 2). The site is an embayment situated deep inland from the west coast, with an area of approximately 0.3 km^2, and it is a unique geographic feature that is formed without large rivers [26].

A DJI Phantom 4 UAV was used to perform the image acquisitions. The UAV overlap images were acquired from the first to sixth time-step (at 14:20, 15:50, 16:30, 17:10, 17:50, and 18:30 on August 12, 2016) at the onset of high tide from low tide. The image acquisition was conducted with a nadir-looking flight in blocks of seven strips at every time-step. The UAV and camera specifications and the overall flight conditions are briefly described in Table I.

The photogrammetric process was implemented in Agisoft PhotoScan to obtain the DEMs of the site for each time. The camera parameters were determined using image alignment. At this stage, the camera orientation parameters (position and rotation of the camera) for each image from the onboard GNSS-IMU (inertial measurement unit) data and camera calibration parameters (focal length, principal displacement, and lens distortions) were refined automatically and stored in the EXIF metadata of the images [30].

TABLE I
Specifications of UAV System and Flight Conditions

DJI Phantom 4	Weight (g)	1,380
	Max. speed (m/s)	20
	Flight time (min)	28
Camera	Focal length (mm)	3.61
	FOV(°)	94
	Sensor size (pix.)	4000 × 3000
Flight Conditions for Each Time-step	Number of images	234–255
	Overlap (%)	80–85 / 75–80
	Altitude (m)	97–104
	GSD (cm/pix.)	3.3–3.7

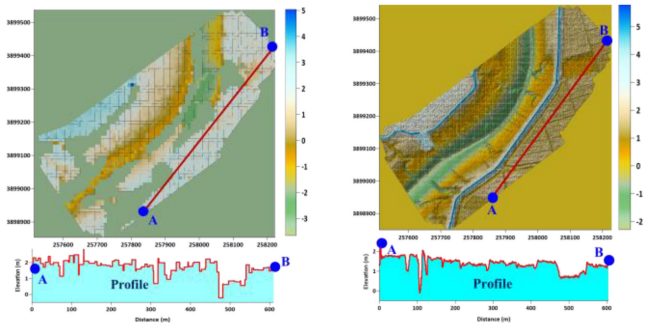

Fig. 3. DEMs derived from TanDEM-X DEM (left) and LiDAR DEM (right). Lines A and B show profiles for comparison with the UAV-DEM morphology.

However, we used the first DJI Phantom 4 model, which has a low-grade GNSS-IMU and an unstable rolling shutter. This may have caused distortion in the recorded images, which became more severe during the standard self-calibration and bundle-adjustment process when using only the tie-points without GCPs. Because of this, location errors were very likely to occur, as well as bowl-shaped distortion in the UAV DEM for a corridor type such as a tidal-channel area, even if photogrammetric software could reduce the distorting effects [20], [21].

We created a TanDEM-X DEM for use as a reference DEM. When creating the DEM using the interferometric SAR technique, we used TanDEM-X data acquired with a very long baseline (1280 m acquired on June 12, 2015) to generate a more accurate DEM over the tidal flats. Because the height variation is not large over the tidal flat, the longer the baseline, the lower the ambiguity height, and thus the accuracy of the generated DEM can be greatly improved. We also selected only points with high coherence, which minimized the occurrence of outliers, and the vertical RMSE of each pixel was maintained to be minimized. In fact, the RMSE of the TanDEM-X DEM we generated over our study area was within 0.27 m. Fig. 3 shows the generated TanDEM-X DEM (resolution 10 m; obtained in 2015) and LiDAR DEM (resolution 1 m; obtained in 2011) used to evaluate the accuracy of the rectified UAV DEM.

Using the dense stereo matching of Agisoft PhotoScan, 10-cm resolution DEMs and 5-cm resolution orthomosaic images were generated using the UAV images. As shown in Fig. 4(a)–(f), the seawater region of the DEMs was an outlier because the image matching was not performed well in the seawater area. Here,

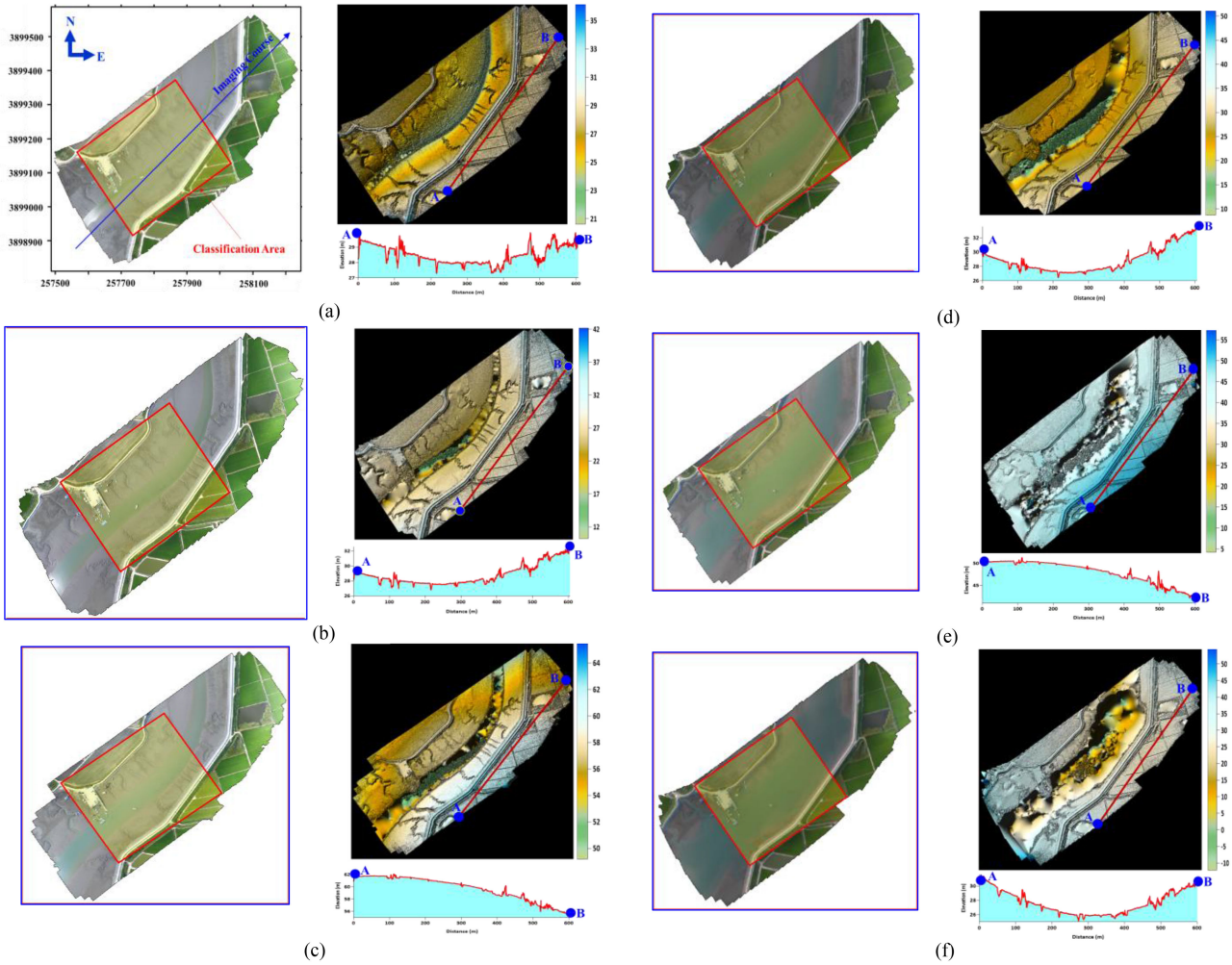

Fig. 4. Orthomosaic images and DEMs derived from UAV-based overlapped images (a)–(f). (a) First time-step. (b) Second time-step. (c) Third time-step. (d) Fourth time-step. (e) Fifth time-step. (f) Sixth time-step.

the produced DEMs were approximately 25–55 m higher than the Tandem-X DEM. It can be visually recognized that all the profiles of the UAV-DEM in Fig. 4 (lines A to B) have a bowl effect with a concave or convex shape compared to the Tandem-X and LiDAR DEMs in Fig. 3. This phenomenon seemed to occur more frequently with an increase in the amount of water in the DEMs.

In the first time-step's orthomosaic image shown in Fig. 4(a), the blue line (imaging course) is the direction for the polynomial models of the transformation parameters. Note that the UAV, TanDEM-X, and LiDAR DEMs are all digital surface models that represent the mean sea-level elevations of the reflective surfaces of all the features. The difference between the three types of DEMs due to vegetation was not large because most of the test area was covered with tidal flats, and the data included roads, paddy fields, and wildland.

The orientation calibration parameters of the camera affected the accuracy of the DEM and orthoimages derived using UAV photogrammetry [20]. The parameters were calculated using the GNSS-IMU on the DJI Phantom 4 and the bundle-adjustment algorithm of Agisoft PhotoScan, but they were inaccurate. GCPs would have to be installed and surveyed on the tidal flat area to obtain an accurate DEM and orthoimage using the refined camera parameters. On the other hand, a survey of GCPs was almost impossible because access to this muddy tidal flat on the southwest coast was very difficult. Therefore, in this study, the produced DEMs were corrected with a presecured TanDEM-X DEM using the LS3D-PM matching method. In the implementation, the diagonal direction [blue line on the DEM in Fig. 4(a)] was used as the flight path of the UAV DEM to determine the polynomial models of the transformation. To compare the DEMs before and after matching in the test area, 25 m to 55 m—mean height difference between the TanDEM-X DEM and each UAV DEM—were subtracted from each original DEMs, as shown in Fig. 4.

A. *First Time-Step DEM Correction*

The first test was used to determine the optimal polynomial model for the LS3D-PM matching using the first time-step's UAV DEM. The model test was applied to a second-order polynomial with the following five cases to obtain the transformation

TABLE II
HEIGHT DEVIATIONS BETWEEN LIDAR DEM AND FIRST TIME-STEP'S UAV DEM BEFORE AND AFTER CORRECTION

Correction	Before	After: Case #				
		1	2	3	4	5
RMSE (m)	0.87	0.82	0.35	0.48	0.29	0.64
Max (m)	3.82	3.47	3.65	3.64	3.33	3.54

parameters. This is why the accuracy did not improve in the higher-order model.

Case 1: 7 parameters ($t_{x0},\ t_{y0}, t_{z0},\ \omega_0,\ \varphi_0,\ \kappa_0,\ s$)
Case 2: 10 parameters ($t_{x0},\ t_{y0}, t_{z0},\ t_{x1},\ t_{y1}, t_{z1},\ \omega_0, \varphi_0, \kappa_0,\ s$)
Case 3: 13 parameters ($t_{x0},\ t_{y0}, t_{z0},\ t_{x1},\ t_{y1}, t_{z1},\ \omega_0$,$\varphi_0, \kappa_0,\ \omega_1, \varphi_1, \kappa_1,\ s$)
Case 4: 13 parameters ($t_{x0},\ t_{y0}, t_{z0},\ t_{x1},\ t_{y1}, t_{z1},\ t_{x2},\ t_{y2}$, $t_{z2},\ \omega_0\varphi_0, \kappa_0,\ s$)
Case 5: 16 parameters ($t_{x0},\ t_{y0}, t_{z0},\ t_{x1},\ t_{y1}, t_{z1},\ t_{x2},\ t_{y2},$, $t_{z2},\ \omega_0\varphi_0, \kappa_0,\ \omega_1$,$\varphi_1, \kappa_1,\ s$).

Fig. 5 shows the iteration behavior of the estimated constant terms of the polynomial model (i.e., the shift and rotation differences) for the five cases. The scale factor results were almost equal to 1.0 in all the cases. Therefore, the scale representation was omitted. In Case 3, the process had the shortest convergence time. The iteration patterns of the estimated parameters were similar in Cases 2, 3, 4, and 5, whereas the behavior of rotation angle κ slightly diverged after iteration 12 in Case 1.

The DEM produced for the first time-step was corrected using the transformation parameters through the proposed LS3D-PM matching, which was based on five cases using the TanDEM-X DEM as the reference DEM. The errors between the DEMs before and after the correction were compared by subtracting the height of the original DEM from the overall elevation difference compared to the LiDAR DEM. Fig. 6 shows a visual comparison before and after the correction for Cases 1 and 4, as well as the profiles (lines A and B). This area is the same as the experimental area of the previous paper [26], but the application of the algorithm and reference DEM for UAV DEM correction is different, as mentioned in the introduction. Therefore, the experimental results presented in Fig. 6 are also different. In the color maps in Fig. 6, the original and Case 1 DEMs are lower than the LiDAR DEM in the central part and higher in the outer part, whereas the heights of the Case 4 DEM were closer to that of the LiDAR DEM. The DEMs in Cases 3 and 5 still showed parabolic distortion, as in Case 1, even though it was omitted in the figure. These comparisons were also omitted because the DEMs corrected for Cases 2 and 4 were similar.

Table II compares each rectified DEM with the LiDAR DEM within the tidal flat area. The error before the DEM correction was 0.9 m, with a maximum error of 3.8 m. The error in the DEM was excessively large compared to that of the LiDAR DEM. The reason seemed to be the mispositioning of some tie-points in water-containing areas for Agisoft PhotoScan as a result of using the SfM technique without GCPs, as well as an unstable rolling shutter of the UAV. It had the potential to cause gross errors and bowl-shaped distortion in the DEM through inaccurate self-calibration and error propagation during the bundle adjustment. After the DEM correction, the RMSE and maximum error fell slightly to 0.8 m and 3.5 m, respectively, for Case 1. The accuracy only improved slightly compared with Case 2.

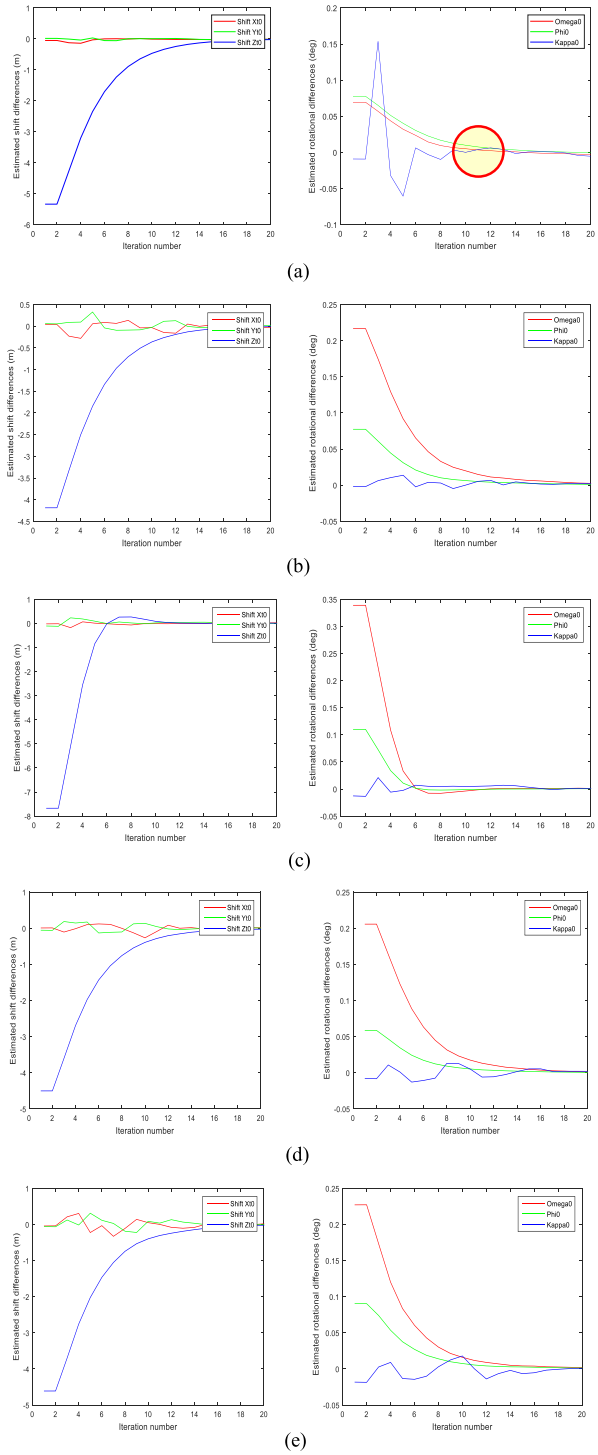

Fig. 5. Convergence behavior of matching algorithm. (a) Case 1. (b) Case 2. (c) Case 3. (d) Case 4. (e) Case 5.

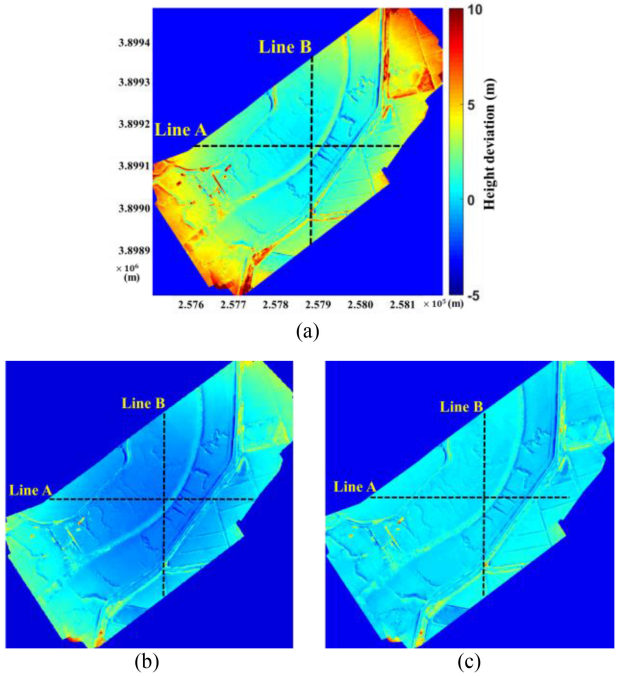

Fig. 6. DEM differences (a) before and after correction for (b) Case 1 and (c) Case 4. The figures are color maps of the height deviations between the UAV DEMs and LiDAR DEM (in meters). The dashed lines (lines A and B) are the profiles for error checking.

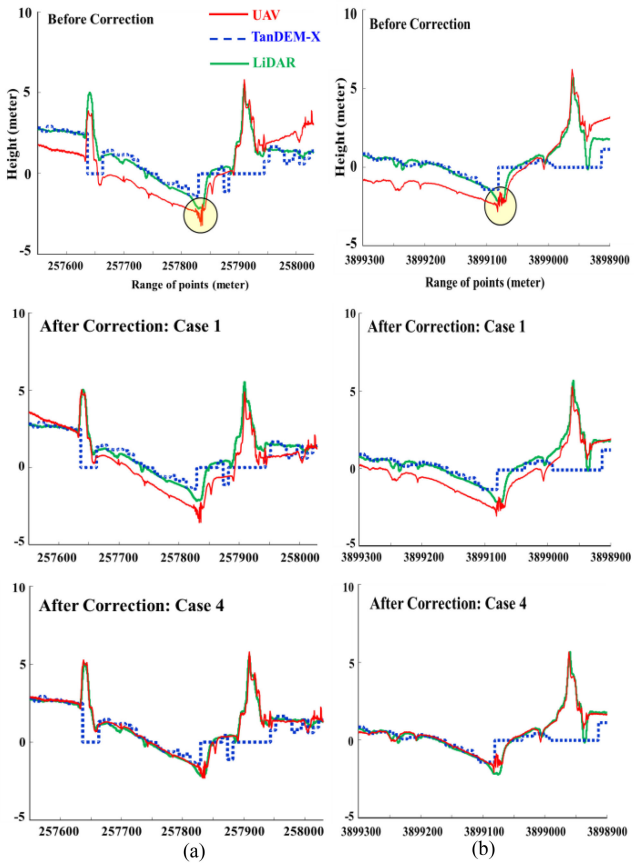

Fig. 7. Profiles before and after correction from UAV DEMs, TanDEM-X DEM, and LiDAR DEM for Cases 1 and 4. The circled section on the red profile before correction shows the error zone in the UAV DEM due to the inflow of seawater in the tidal channel. (a) Profiles on Line A. (b) Profiles on Line B.

Nevertheless, the DEM was still relatively large compared to the DEM resolution (10 cm). This could be explained by an artificial difference (e.g., a small boat in the tidal flats and puddle); topographic changes in some spots (e.g., sedimentation and erosion) between the two types of data over the five-year time-variance, as shown in Fig. 6(c); and mismatched points as a result of reflection from an underwater area, where the seawater flowed into the tidal channel at high tide during the process of stereo matching.

For a detailed comparison of the corrected DEMs, the profiles were visualized, and the errors between the UAV and LiDAR profiles were computed. Fig. 7 shows the pattern difference in each case between the LiDAR, TanDEM-X DEM, and UAV DEM before and after correcting the profiles on lines A and B, as shown in Fig. 6(a).

In the case of the TanDEM-X DEM, voids occurred in the embankment and water area, as shown in Fig. 3(left). Therefore, in the tidal flat section, except for these areas, it can be seen that it was almost identical to the LiDAR DEM.

The accuracy was evaluated using the pattern difference and height deviation between the two profiles of the corrected UAV DEM and LiDAR DEM.

The deformation still existed because of the bowl effect even after the correction, despite the smaller errors in Case 1 compared to the original UAV DEM in Fig. 7. It was observed that there was also a slight distortion when applying the parameters of Cases 2 and 3. This error was removed in Case 4, whereas it occurred in Case 5. The error could still be found in Case 5, whereas Case 4 showed almost no discrepancy. Accordingly,

TABLE III
HEIGHT DEVIATIONS BETWEEN LIDAR AND FIRST TIME-STEP UAV DEM BEFORE AND AFTER CORRECTION ON LINES A AND B PROFILES IN FIG. 4

Correction		Before	After: Case #				
			1	2	3	4	5
Profile A	RMSE (m)	1.14	0.70	0.13	0.31	0.13	0.37
	Max (m)	1.65	1.21	0.51	0.68	0.45	0.75
Profile B	RMSE (m)	0.96	0.81	0.16	0.27	0.07	0.29
	Max (m)	1.81	1.11	0.45	0.72	0.45	0.84

the translation parameters in the LS3D-PM matching method required a model with a higher order than the linear polynomial with an increase in the DEM grid space to remove the bowl-shaped distortion of the DEM produced without GCP surveying. Meanwhile, rotation only required the zero-order parameter, but higher-order parameters caused distortion in the 3-D surface matching.

Table III lists the calculated height differences within the tidal flat area for the profiles shown in Fig. 7. The RMSE decreased sharply from Case 2 compared to that before the correction, whereas the RMSE in Case 3 increased compared to that in Case 2. The accuracy was slightly improved in Case 4

compared to Cases 2 and 3. Similar to Case 5, however, applying higher-order polynomial parameters in Case 4 produced inferior results because of the limitation of the TanDEM-X DEM as reference data, which had null values in the blank area, as shown in Fig. 3(left). It was surmised that the optimal parameter to correct the UAV-made DEM while using the reference DEM and proposed LS3D-PM matching method was Case 4, which was similar to the bowl effect geometry. This included a curved polynomial and constant model for the shift and rotation, respectively.

The RMSE through the implementation was approximately 10 cm while the RMSE was nearly 15 cm in the case of the LHD matching [26]. The reason is that even LiDAR DEM is used as the reference DEM, the LHD is inferior in the steep tidal-channel area. Although the TanDEM-X DEM, which has lower accuracy and resolution than LiDAR DEM, was employed as the reference DEM in the steep area, it seems that the parameters were able to obtain more slightly accurate results due to the robustness of the proposed technique. The experimental results showed that the proposed technique reduced the error of the DEM produced with the UAV and photogrammetric software using only the reference DEM, and eliminated the error caused by the bowl effect without surveying GCPs.

B. Multitime DEM Corrections and Seawater Change Estimations

In the second test, all the UAV DEMs were rectified using the optimal parameter of the proposed method with the corrected first time-step UAV DEM. Consequently, the changes in the seawater level and area were estimated using the corrected DEMs and orthoclassified images. Fig. 8 presents the results before and after correcting the UAV images on the mesh of the LiDAR DEM in a lateral view of the 3-D surface. Here, each uncorrected DEM was also subtracted from the overall height bias with the LiDAR DEM. All the DEM corrections were performed using the polynomial model selected in the first test, i.e., Case 4. The original UAV DEMs were almost parabolic in shape. In particular, in the third and fifth time-step DEMs, reverse bowl-shaped distortion occurred, in contrast to the other DEMs. The form of the distortion may be determined by the types (pincushion or barrel) of the radial distortion according to the scale changes from the central image to the edges due to the propagated systematic errors through the inaccurate bundle adjustment. The original meshes were inconsistent with the LiDAR mesh, whereas the corrected DEMs closely matched the LiDAR mesh. This suggested that the original UAV DEM could be properly compensated using the proposed method, even if the errors and shapes due to the bowl effect were significantly large and different, based on the experimental results.

Profiles were created to investigate the correction accuracies of the DEMs at each time point. Fig. 9 shows the height profile disparities at each time point between the LiDAR and UAV DEMs before and after correcting the line A profile. Large profile errors occurred at the third–sixth time-step DEMs compared to the first and second time-step DEMs. During the photogrammetric software process, mismatched points occurred

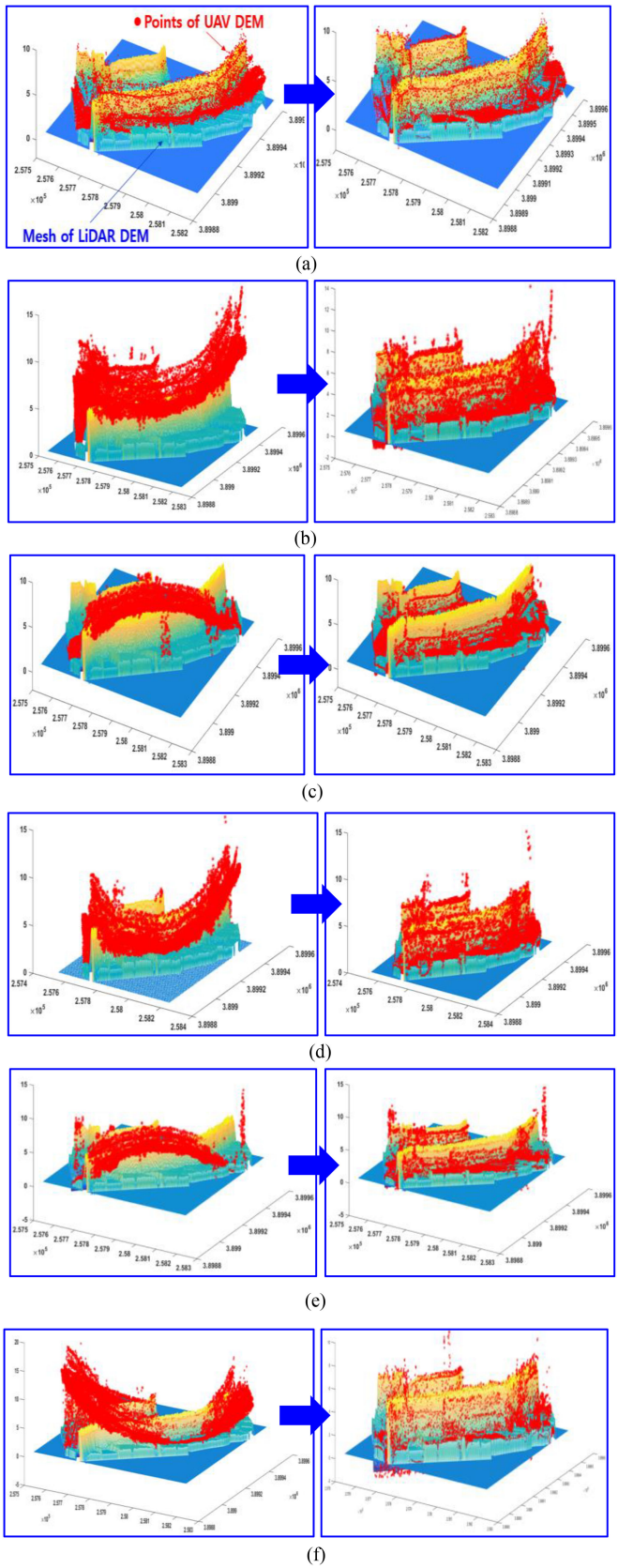

Fig. 8. Figures overlaid with UAV point clouds and LiDAR mesh. Before (left columns) and after correction (right columns) for each time-step UAV DEM. (a) First time-step. (b) Second time-step. (c) Third time-step. (d) Fourth time-step. (e) Fifth time-step. (f) Sixth time-step.

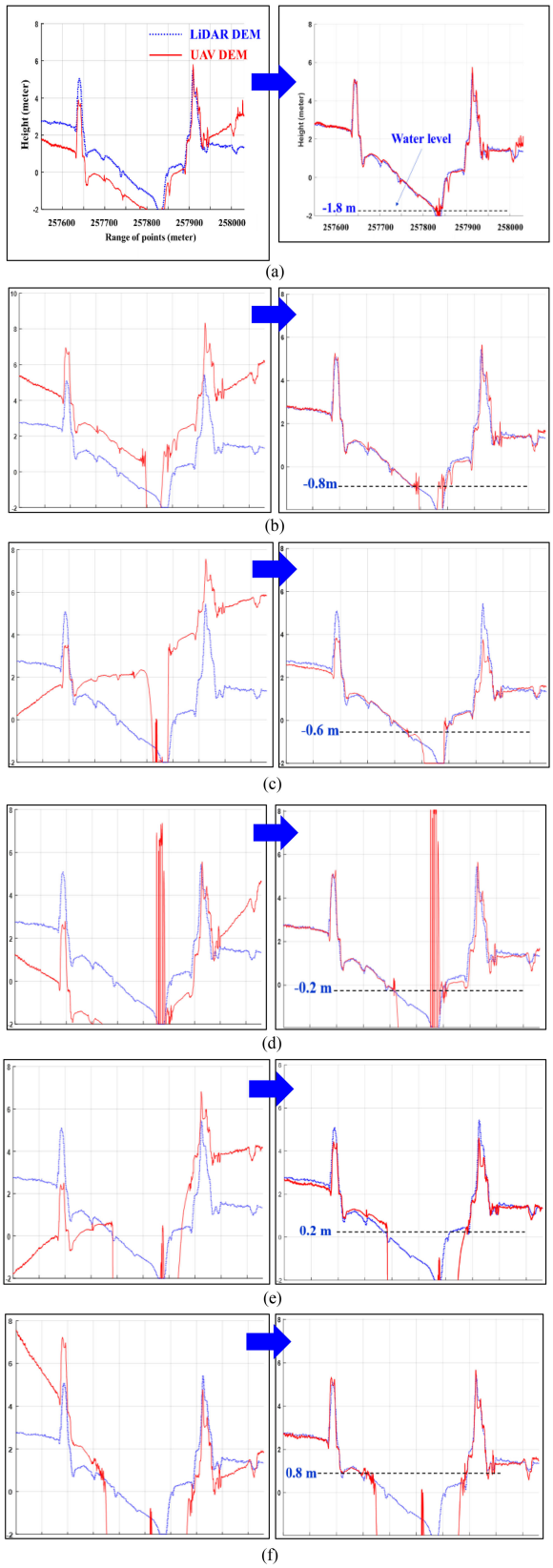

Fig. 9. Profiles before (left columns) and after correction (right columns) for each time-step UAV DEM. Red line: UAV DEM profiles. Blue line: LiDAR DEM profiles. The dashed lines in the right column are seawater heights. (a) First time-step. (b) Second time-step. (c) Third time-step. (d) Fourth time-step. (e) Fifth time-step. (f) Sixth time-step.

TABLE IV
HEIGHT DEVIATIONS BETWEEN LIDAR AND EACH TIME-STEP UAV DEM ON LINE A PROFILE IN FIG. 6

Correction	RMSE (m)				
	Second	Third	Fourth	Fifth	Sixth
Before	1.5	1.6	2.6	0.9	0.9
After	0.1	0.2	0.1	0.2	0.1

in the overlapped images of the inflow water region where the water level increased as the high tide progressed. Some profiles had large errors compared with the LiDAR DEM (a minimum height of −2.3 m), including the outliers due to mismatching [see Fig. 9(d)]. Nevertheless, the corrected DEM profiles corresponded remarkably well with the LiDAR DEM profile.

Table IV lists the profile errors within the only tidal flat zone, excluding the water area on the line A profile, between the DEMs of the second–sixth time-steps and the LiDAR DEM. The RMSEs before the DEM correction were approximately 1–3 m. After the DEM correction, the RMSE values fell to 0.1–0.2 m. Overall, the errors of the proposed matching did not exceed 0.2 m in all the corrected DEMs in the tidal range.

To estimate the seawater changes in the tidal channel, classified images were manufactured using the maximum-likelihood method in the ERDAS IMAGINE software. A classification image could be made using orthoimages obtained with a UAV equipped with a near-infrared camera, but this implementation was based only on the trial approach. The original orthoimages could be compensated using the corrected DEMs and the ERDAS Autosync tool.

Classification images for each time-step were also produced using the corrected orthoimages. The classification was performed using the maximum-likelihood method, which is commonly used. The categories were water, mud-wildland, vegetation, and concrete, with a focus on water and nonwater area classification. The overall classification accuracy was between 83% and 93% for all six time-steps. The classified images could be used to interpret the changes in the water area, as well as the changes in the water boundary height, by overlapping the contours of the corrected DEMs, as shown in Fig. 10.

The seawater level was measured using two approaches. First, line A profiles were used in the corrected DEMs of each time-step. As shown in Fig. 4, because image matching was not properly carried out in the seawater area, outlier heights occurred at this location. Therefore, the boundary of this part was considered to be the seawater level. Fig. 9 shows the estimated seawater heights at each time. Second, the seawater level could be measured by superimposing the classified-images of each time-step and the contour line of the corrected DEM for the first time-step. The DEM of this time-step was used because the seawater level of this DEM was the lowest, and the bottom surface was the most exposed. The seawater area could be measured by counting the number of water designations in the classified image. Fig. 10 shows the subset of orthomosaic images and classified images from the original images for each

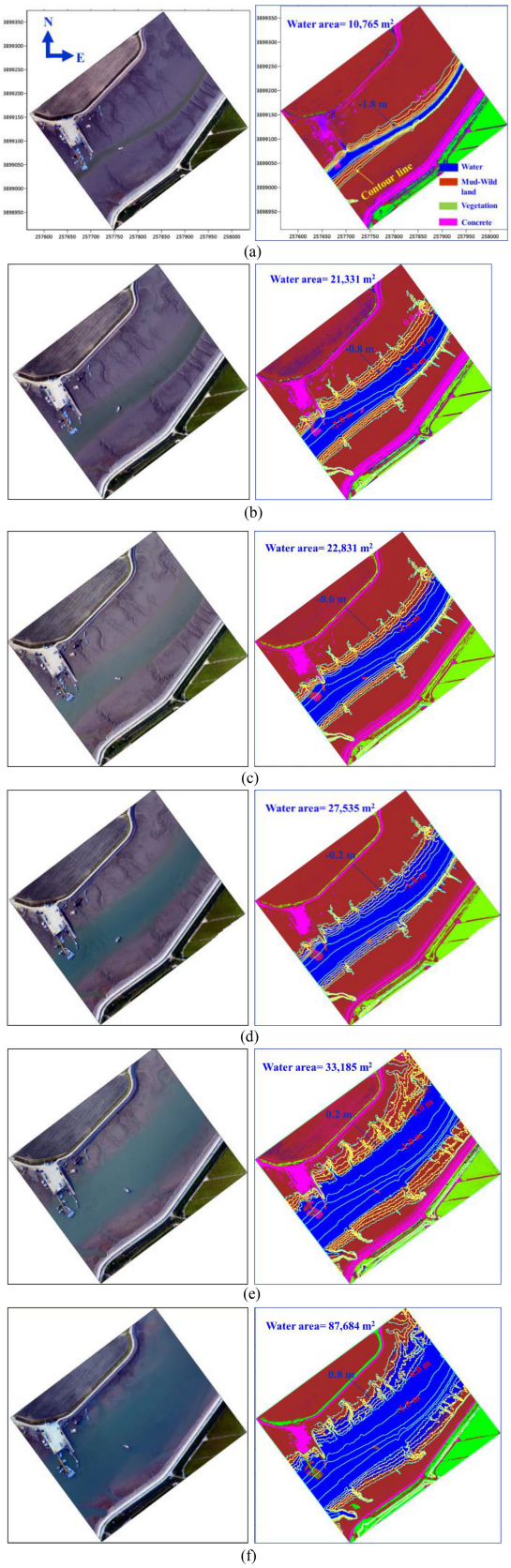

Fig. 10. Orthomosaic images (left column), classification images, and contour lines (right columns) in subset red-box region in Fig. 4 for each time-step. (a) First time-step. (b) Second time-step. (c) Third time-step. (d) Fourth time-step. (e) Fifth time-step. (f) Sixth time-step.

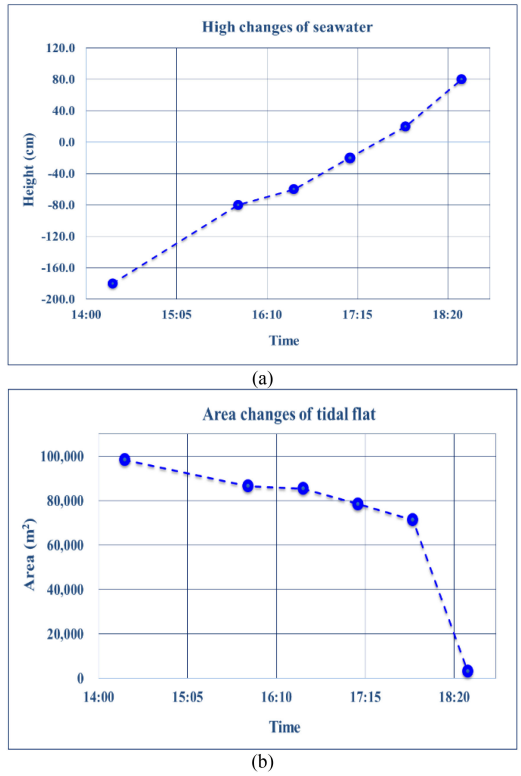

Fig. 11. Changes in (a) tidal height and (b) tidal area over time.

time-step, which was used to estimate the changes in seawater in the same area. In particular, the water area showed a sharp increase at the sixth time-step.

The seawater height could be determined by matching the seawater boundary line and the contour line in the classification image (see Fig. 10). The determined heights were almost in line with the previously predicted heights (right column in Fig. 9). Therefore, the seawater level was confirmed using the two approaches, as shown in Fig. 11, along with the exposed tidal flat area.

On the other hand, the measured heights were also related to the errors in the corrected DEM and profiles. An area was measured by classifying it using a normal RGB camera image. Therefore, although the area was not accurate, the tendency for the seawater area to change could be analyzed. As shown in Fig. 11, the tidal flat area decreased steeply after 5 pm while the height showed a constant upward curve. One of the reasons is that the slope of the area is approximately 2%, which is close to flat topography. Therefore, the speed that the area disappeared increased rapidly after 5 P.M. during the flooding tide in the test area (i.e., it was recognized that the sea level rose rapidly approximately 3 h after the seawater first entered).

IV. Conclusion

Tidal flats are unique ecosystems that provide habitats for various species and purify pollutants discharged from land areas. Due to these unique characteristics, recreational activities

have increased recently in the tidal flats, and in the meantime, accidents sometimes occur where people cannot get out at high tide. Thus, regular observation and mapping of high-precision DEM of the tidal flats are needed to detect water level changes along the tidal channels. However, it is very difficult to conduct a survey because these regions have high moisture contents and consist mostly of silt, clay, and sand, making it difficult for an observer to approach and move around in the field. This study showed that DEMs and orthoclassified images could be produced using UAV images and SfM-based photogrammetric software to estimate water level changes at a tidal channel site. However, it is difficult to collect GCPs in tidal flats to produce an accurate DEM. This article proposed an LS3D-PM DEM matching technique that used a TanDEM-X DEM for reference data and removed the bowl-effect error of the original DEMs without a GCP field survey in a tidal channel.

The implementation was performed in five cases with different correction models to determine the optimal model for the proposed technique. In the experimental investigations, an optimal model was determined, in which the translation was a second-order parameter, and the rotation was a zero-order parameter as the number of DEM grids increased in the flight direction. The RMSE in this case was approximately 10 cm. This result was close to the DEM resolution (10 cm) from the acquired UAV image. The experimental results showed that the proposed method could reduce the error in a tidal flat DEM using only the reference DEM, as well as eliminate the bowl-effect error. This method was quite effective at correcting the DEM produced using UAV images obtained in inaccessible areas, where GCP surveys would be difficult. Furthermore, it was possible to avoid the uncertainty in the measurement of the image coordinates, which leads to errors in the produced DEM.

Using the corrected DEM and orthoclassified images, the changes in the seawater and exposed tidal area during flooding tide over time could be determined quantitatively. The limitation of this experimental result was that the accuracy of the exposed tidal flat changes over time depended on the overall error of the corrected DEM. Nevertheless, through these experimental results, it would be possible to determine the peak time of the tidal invasion in other regions, as well as that of the tidal channel in the study region. In addition, visual data produced using the proposed method, as shown in Fig. 11, could help prevent accidents in a tidal flat. Valuable data could also be provided for analyzing the geographical features of tidal channels.

Acknowledgment

The authors would like to thank the German Aerospace Center (DLR) for providing TanDEM-X data via the TDX Project ATI_OCEA0391 to DJK.

References

[1] R. T. Reppert, W. Sigleo, E. Stakhiv, L. Messman, and C. Meyers, "Wetland values: Concepts and methods for wetlands evaluation," U.S. Army Corps Eng. Inst. Water Res., Alexandria, VA, USA, Tech. Rep. 79-R1, 1979.

[2] C. H. Koh and J. S. Khim, "The Korean tidal flat of the Yellow Sea: Physical setting, ecosystem and management," *Ocean Coast. Manage.*, vol. 102, pp. 398–414, Dec. 2014.

[3] Yonhap News Agency, Korea. Accessed: Nov. 11, 2020. [Online]. Available: https://www.yna.co.kr/view/AKR20201111069900054

[4] R. M. Myrick and L. B. Leopold, "Hydraulic geometry of a small tidal estuary," U.S. Geological Survey, Reston , VA, USA, Tech. Rep. 422-B, Aug. 1963.

[5] Z. J. Hughes, "Tidal channels on tidal flats and marshes," in *Principles of Tidal Sedimentology*, R. Davis Jr. and R. Dalrymple, Eds. Dordrecht, The Netherlands: Springer, 2012, pp. 269–300. [Online]. Available: https://link.springer.com/chapter/10.1007/978-94-007-0123-6_11

[6] C. Wimmer, R. Siegmund, M. Schwäbisch, and J. Moreira, "Generation of high precision DEMs of the Wadden sea with airborne interferometric SAR," *IEEE Geosci. Remote Sens.*, vol. 38, no. 5, pp. 2234–2245, Sep. 2000.

[7] P. H. Ross, S. L. Ustin, and A. Hastings, "Use of LiDAR to study changes associated with Spartina invasion in San Francisco bay marshes," *ISPRS J. Photogramm.*, vol. 100, pp. 295–306, Feb. 2006.

[8] J. H. Oh, D. J. Kim, and H. S. Lee, "Topographic information extraction of tidal flats using remote multi-sensory data," *J. Coast. Res.*, vol. 91, pp. 371–375, Aug. 2019.

[9] KHOA, Korea. Accessed: Sep. 9, 2021. [Online]. Available: https://www.khoa.go.kr

[10] J. S. Won, Y. H. Na, and S. W. Kim, "Tidal flat DEM generation by satellite remote sensing," in *Proc. Int. Geosci. Remote Sens. Symp.*, 2003, pp. 2116–2118.

[11] D. J. Kim, W. M. Moon, G. B. Kim, S. E. Park, and H. S. Lee, "Submarine groundwater discharge in tidal flats revealed by space-borne synthetic aperture radar," *Remote Sens. Environ.*, vol. 115, pp. 793–800, Feb. 2011.

[12] K. L. Kim, B. J. Kim, Y. K. Lee, and J. H. Ryu, "Generation of a large-scale surface sediment classification map using unmanned aerial vehicle (UAV) data: A case study at the Hwang-do tidal flat," *Remote Sens.*, vol. 11, pp. 1–15, Jan. 2019.

[13] M. Jaud et al., "Potential of UAVs for monitoring mudflat morphodynamics (application to the Seine Estuary, France)," *ISPRS Int. J. Geo Inf.*, vol. 5, pp. 1–20, Apr. 2016.

[14] N. Long, B. Millescamps, B. Guillot, F. Pouget, and X. Bertin, "Monitoring the topography of a dynamic tidal inlet using UAV imagery," *Remote Sens.*, vol. 8, no. 5, pp. 1–18, 2016, doi: 10.3390/rs8050387.

[15] EcoSea, Korea. Accessed: Dec. 3, 2019. [Online]. Available: http://www.ecosea.go.kr

[16] M. M. Ouédraogo, A. Degré, C. Debouche, and J. Lisein, "The evaluation of unmanned aerial system-based photogrammetry and terrestrial laser scanning to generate DEMs of agricultural watersheds," *Geomorph*, vol. 214, pp. 339–355, 2014.

[17] M. R. James and S. Robson, "Mitigating systematic error in topographic models derived from UAV and ground-based image networks," *Earth Surf. Processes Landforms*, vol. 39, pp. 1413–1420, Jun. 2014.

[18] F. Da, C. Nogueira, L. Roberto, T. S. Körting, and E. H. Shiguemori, "Accuracy analysis of orthomosaic and DSM produced from sensor aboard UAV," in *Proc. Int. Braz. Symp. Remote Sens.*, 2017, pp. 5515–5525.

[19] M. Jaud et al., "Assessing the accuracy of high resolution digital surface models computed by Photoscan and Micmac in sub-optimal survey conditions," *Remote Sens.*, vol. 8, no. 6, pp. 1–18, 2016, doi: 10.3390/rs8060465.

[20] S. Gindraux, R. Boesch, and D. Farinotti, "Accuracy assessment of digital surface models from unmanned aerial vehicles' imagery on glaciers," *Remote Sens.*, vol. 9, no. 2, pp. 1–15, 2017, doi: 10.3390/s9020186.

[21] Y. Zhoul, M. Daakir, E. Rupnik, and M. Pierrot- Deseilligny, "A two-step approach for the correction of rolling shutter distortion in UAV photogrammetry," *ISPRS J. Photogramm. Remote Sens.*, vol. 160, pp. 51–66, 2020.

[22] G. Markus and P. Heinz-Jürgen, "Accuracy analysis of photogrammetric UAV image blocks: Influence of onboard RTK-GNSS and cross flight patterns," *PFG J. Photogramm. Remote Sens Geoinformation Sci.*, vol. 1, pp. 17–30, 2016.

[23] Y. Taddia, F. Stecchi, and A. Pellegrinelli, "Using DJI PHANTOM 4 RTK drone for topographic mapping of coastal areas," in *Proc. Int. Arc. Photogram. Remote Sens. Spatial Inf. Sci.*, 2019, pp. 625–630.

[24] P. J. Besl and N. D. Mckay, "A method for registration of 3-D shapes," *IEEE Trans. Pattern Anal. Mach. Intell.*, vol. 14, no. 2, pp. 239–256, Feb. 1992.

[25] A. Gruen and D. Akca, "Least squares 3D surface and curve matching," *ISPRS J. Photogramm. Remote Sens.*, vol. 59, no. 3, pp. 151–174, May 2005.

[26] H. S. Lee and D. Y. Han, "Rectification of bowl-shape deformation of tidal flat DEM derived from UAV imaging," *Sensors*, vol. 20, no. 6, pp. 1–14, 2020, doi: 10.3390/s20061602.

[27] G. Karras and E. Petsa, "DEM matching and detection of deformation in close-range photogrammetry without control," *Photogramm. Eng. Remote Sens.*, vol. 59, no. 9, pp. 1419–1424, Sep. 1993.
[28] T. Schenk, A. Krupnik, and Y. Postolov, "Comparative study of surface matching algorithms," in *Proc. Int. Arc. Photogram. Remote Sens.*, 2000, pp. 518–524.
[29] B. Wessel, M. Huber, C. Wohlfart, U. Marschalk, D. Kosmann, and A. Roth, "Accuracy assessment of the global TanDEM-X digital elevation model with GPS data," *ISPRS J. Photogramm. Remote Sens.*, vol. 139, pp. 171–182, 2018.
[30] Agisoft PhotoScan User Manual. Agisoft LLC, 2018. Accessed: Dec. 30, 2019. [Online]. Available: https://www.agisoft.com/pdf/photoscan-pro_1_4_en.pdf

Hyoseong Lee received the B.S., M.S., and Ph.D. degrees from the Department of Civil Engineering, Gyeongsang National University, Jinju, South Korea, in 1995, 1997, and 2000, respectively.

He has performed researches about digital photogrammetry as a postdoctoral researcher with the Department of Civil and Environmental Engineering and School of Earth and Environmental Sciences, Seoul National University, Seoul, South Korea, for 6 years before joining Sunchon National University as a Professor in 2006. His research interests include digital photogrammetry and its application in various fields such as the 3-D construction measurement by stereo camera images as well as the precise digital mapping using satellite images.

Duk-jin Kim (Senior Member, IEEE) received the B.Sc. degree in Earth system science and the M.Sc. and Ph.D. degrees in radar remote sensing and geophysics from Seoul National University, Seoul, South Korea, in 1999, 2001, and 2005, respectively.

From October 2005 to July 2007, he was a Postdoctoral Researcher with the University of Manitoba, Winnipeg, MB, Canada, and with the University of Michigan, Ann Arbor, MI, USA. From July 2007 to August 2008, he was a Senior Researcher with the Remote Sensing Division, Korea Aerospace Research Institute, Daejeon, South Korea. He is currently a Full Professor with the School of Earth and Environmental Sciences, Seoul National University. During his sabbatical leave from August 2014 to July 2015, he joined as a Visiting Scholar with the Radar Science and Engineering Section, Jet Propulsion Laboratory, California Institute of Technology, Pasadena, CA, USA. His research interests include coastal environment and disaster monitoring using space-borne and airborne synthetic aperture radar (SAR) systems, as well as Earth's physical parameter extractions using along/cross-track interferometric and polarimetric SAR data. His current research interests include automatic disaster monitoring and global environment change monitoring using cloud-computing and AI technology.